INVITED REVIEW

Applications of parametric processes to high-quality multicolour ultrashort pulses, pulse cleaning and CEP stable sub-3fs pulse

Takayoshi Kobayashi[1,2,3,4,5]**, Jun Liu**[1,2,3,6] **and Kotaro Okamura**[1,3,7]

[1] Advanced Ultrafast Laser Research Center, University of Electro-Communications, Chofugaoka 1-5-1, Chofu, Tokyo 182-8585, Japan
[2] Core Research for Evolutional Science and Technology (CREST), Japan Science and Technology Agency, K's Gobancho, 7, Gobancho, Chiyoda-ku, Tokyo 102-0076, Japan
[3] JST, ICORP, Ultrashort Pulse Laser Project, K's Gobancho, 7, Gobancho, Chiyoda-ku, Tokyo 102-0076, Japan
[4] Department of Electrophysics, National Chiao Tung University, 1001 Ta Hsueh Rd. Hsinchu 300, Taiwan
[5] Institute of Laser Engineering, Osaka University, 2-6 Yamada-Oka, Suita, Osaka 565-0871, Japan
[6] State Key Laboratory of High Field Laser Physics, Shanghai Institute of Optics and Fine Mechanics, Chinese Academy of Sciences, Shanghai 201800, People's Republic of China

E-mail: jliu@siom.ac.cn

Abstract

Our recent experimental results of three methods related to and useful for the generation of attosecond pulses are summarized. The pulses obtained by all of them have high qualities in terms of phase, temporal, spectral and spatial properties which are based on the physical principles associated with the parametric processes. First, carrier-envelope phase (CEP) stable sub-5 fs and sub-3 fs pulses by non-collinear optical parametric amplification (NOPA) in the near-infrared and visible spectral range will be described. The mechanism of the passive CEP stabilization is described. Passively stabilized idler and its second harmonic (SH) pulses from NOPAs are compressed to sub-5fs and sub-3fs, respectively. Compression of the idler output from a NOPA and its SH is attained with a specially designed characterization method during the compression. Second, generation of multicolour pulses by the cascaded four-wave mixing process in bulk media is discussed. As short as 15-fs multicoloured femtosecond pulses are obtained with two ~40 fs pulses incident to a fused-silica glass plate by this method. These broadband multicolour sidebands are expected to provide single-cycle or sub-fs pulses after the Fourier synthesis. Third, a new technique based on self-diffraction in the Kerr medium is used to clean and shorten the femtosecond laser pulse. The cleaned pulse with high temporal contrast is expected to be used as a seed for a background-free petawatt laser system and then used as the laser source for high-energy attosecond pulse generation in a solid target. The mechanisms of CEP stabilization, pulse spectral smoothening and pulse contrast enhancement are comparatively discussed.

(Some figures may appear in colour only in the online journal)

[7] Present address: Megaopto Co., Ltd., RIKEN-WAKO Incubation Plaza 301, 2-3-13 Minami, Wako, Saitama 351-0104, Japan.

1. Introduction

In the last decades, lasers generating femtosecond pulses were developed explosively. Sub-5 fs pulses can be generated directly from a Ti:sapphire oscillator [1]. By using self-phase modulation in hollow waveguides or filament, even a 2.6 fs pulse can be obtained by a spatial light modulator to compensate the dispersion [2, 3]. The tunable sub-5 fs pulse was also achieved by a non-collinear optical parametric amplification (NOPA) [4, 5].

On the other hand, based on the chirped pulse amplification (CPA) [6] and optical parametric chirped pulse amplification [7], the femtosecond pulse can be boosted to a terawatt level and even further to a petawatt level [8–11].

Femtosecond laser pulses can be used for the generation of even shorter pulses in attosecond regimes. The attosecond pulse is expected to be used in various applications including the study of attosecond spectroscopy. Spectroscopy will clarify the electron dynamics in atoms and molecules and was already used in pump-probe studies of 1 fs scale electron dynamics [12]. There are three types of methods used to obtain attosecond pulses reported so far. First, high-order harmonic generation (HHG) in gases driven by a few-cycle intense femtosecond laser pulse is the most popular method for attosecond pulse generation [13–16]. In this method, a carrier-envelope phase (CEP) stable pulse with short pulse duration is very important for the generation of a short single attosecond pulse [17–24]. A single 50 attosecond pulse has been generated through HHG driven by a CEP stable sub-5 fs pulse [25, 26]. Second, sub-fs pulses with high pulse energy can be obtained by the method of Fourier synthesis with many line spectra with an equal frequency separation. A method based on coherently enhanced stimulated Raman scattering (SRS) is a typical method in this scheme [27]. A train of pulses as short as 1.6 fs corresponding to a sub-single-cycle pulse duration has been obtained in this way [28–30]. Third, an alternative method is to use solid targets as nonlinear media for HHG. High-energy attosecond or even zeptosecond pulses are predicted to be generated with high efficiency by focusing the intense laser pulses to a solid surface leading to the formation of plasma used as a nonlinear medium [31–35]. In this process, the intensity of the laser pulse reaches the highly relativistic regime. Such an intense pulse with high temporal contrast is important to prevent the generation of preplasma by intense enough prepulses and to maintain the stability of the generated HHG pulse [36].

In this review paper, we will describe our recent experimental results related to the above three methods useful for attosecond pulse generation. First, CEP stable sub-5 fs and sub-3 fs pulses by a NOPA in the near-infrared (NIR) and visible spectral range will be described. CEP stabilization is important to generate a single attosecond pulse by HHG, which is indispensable for a well-characterized pump/probe type experiment. Second, the generation of multicolour pulses by a cascaded four-wave mixing (CFWM) process in bulk media is discussed. The pulse can be shortened in this process. The same as the SRS method, these broadband multicolour sidebands are expected to obtain single cycle or sub-fs pulses

after Fourier synthesis of the sidebands in the near future. Third, a new technique based on self-diffraction (SD) in a Kerr medium is described to clean the femtosecond laser pulse by removing satellite pulses and basal for high-power applications. The cleaned pulse with high temporal contrast is expected to be used as a seed pulse for the background-free petawatt laser system and then used as the laser source for high-energy attosecond generation in a solid target. In the study of short pulse generation by the parametric oscillator or amplifier, it is very important to remove or relax the limitation set by the phase-matching condition to obtain broad enough gain bandwidth. This is shown in section 3 in this paper. From the different viewpoint, the phase-matching condition can be useful for the improvement of properties of output pulses and is shown in sections 1 and 2 in this paper.

2. CEP-stabilized few-cycle pulse generated from NOPA

2.1. Principle of the idea

Controlling CEP slip is critical in the applications for extreme nonlinear optical phenomena such as HHG extending to the soft x-ray region [37, 38], attosecond pulse generation and in precision optical frequency measurement [39]. Many research groups have worked for active stabilization of the CEP of the output from a mode-locked oscillator with a servo-loop feedback system [39–41]. CEP is considered to be the last resource of the optical light pulse. A CEP-sensitive phenomenon was demonstrated first in an experiment on photoelectron emission [42]; recently, CEP dependence was reported in a soft x-ray spectrum generated with a CEP-stabilized intense laser system [12]. It was shown by our group that the self-elimination of pulse-to-pulse CEP slip takes place in the parametric difference frequency amplification systems [43, 44]. An experiment to prove it was performed using a NOPA system [43] pumped with second harmonic (SH) of the fundamental Ti:sapphire radiation and seeded with the white-light continuum produced by the same SH. It was also proved that the CEP stabilization was obtained in a NOPA system pumped with the fundamental Ti:sapphire laser and seeded with the continuum generated by the fundamental [44]. Passive CEP stabilization was also shown in the difference frequency generation [45].

In the OPA process, the phases of all three pulses are related to each other. Typically, the frequencies and phases of the relevant pump, seed and idler (represented by suffixes, P, S and I, respectively) pulses in the three-wave mixing process can be expressed by the following equations in the paper from our group [43]:

$$\omega_I = \omega_P - \omega_S$$
$$\psi_I = -\pi/2 + \psi_P - \psi_S. \tag{1}$$

The SH generation (SHG) process is also a three-wave mixing process. Based on the above expression, the phase of the SHG signal can be expressed by

$$\psi_{SH} = \pi/2 + 2\psi. \tag{2}$$

This expression is widely used in the measurements of the CEP drift, where the beating frequency between the overlapped frequency of the SH and fundamental spectra is measured [44].

From the above expression, the CEP of the idler pulse is automatically stabilized when the seed pulse used for white light generation and the pump pulse is the same pulse. Because of the self-stabilization mechanism this passive method has several advantages over active mechanism invented by Haensch and Hall as follows. The first one is that there is no requirement of octave bandwidth to stabilize the pulse to obtain the beat signal between the fundamental and the second harmonic of the pulse of which CEP is to be stabilized. Therefore, in case the pulse of interest does not have enough bandwidth, it needs to be broadened. The second advantage is that there is no need for sophisticated electronics to control the cavity by the feedback mechanism. The third one is the applicability to the amplifier system. In the case of the passive method, CEP stabilization is attained by the feedback to the cavity mirrors using the beat signal as a source of the error signal which can be applied to an oscillator but not to an amplifier system.

Based on the idea of passive stabilization of CEP, we explored the experiment in the NIR and visible and obtained sub-5 fs in the NIR and sub-3 fs in the visible spectral range. This CEP-stabilized pulse can be utilized in many applications.

2.2. Compensation of dispersion to generate sub-5 fs with CEP stability in the NIR

Before addressing the main subject of the generation of a sub-3 fs CEP-stabilized pulse utilizing the SH of the idler pulse from a NOPA, the report on the generation of a shorter idler fundamental pulse than 5 fs from a NOPA is discussed below [46]. The compression of the fundamental idler was realized by extending the method used in the latter compression of the SH.

Widely used NOPA to obtain ultrashort visible–NIR pulses has been developed by solving the problem of limitation of gain bandwidth of parametric amplification and extensive development has been made by many groups [5, 47–52]. In particular, application of pulse front matching helped to reduce the effect of offset of pulse fronts of the pump and seed, and angular chirped pumping helped to extend the phase-matching angle using a prism. The pulse generated in this way was compressed by several compressors, prism compressor, grating compressor, chirped mirror and deformable mirror, and it has become possible to reach the nearly transform limited pulses [4, 5, 47, 50, 52].

Idler output from a NOPA with passively stabilized CEP by the mechanism described in the previous subsection was compressed to sub-5 fs duration by applying a specially designed characterization method during the compression. The pump and seed of this NOPA are the SH of the amplified pulse and the supercontinuum generated by the SH, respectively. The output of an amplified Ti:sapphire laser operating at the wavelength around 790 nm with about 120 fs duration was frequency doubled to pump the NOPA composed of a 1-mm-thick beta barium borate (BBO) crystal with the cut angle, θ, of

$31°$. The energy of the 395 nm pump pulse was about 9 μJ. The SH pump pulse and the SH-generated supercontinuum pulse were introduced into the NOPA crystal, with an internal non-collinear angle of α_{NC} being $4.7°$ between the two beams. Spatially and temporally overlapped pulses generate idler radiation. The output energies of the signal and idler waves from the BBO crystal were 1.6 and 1.1 μJ, respectively. It is worthwhile to mention that the pump energy was chosen to obtain the necessary amount of the idler-SH to investigate the CEP stability by the interference, while efficient parametric amplification and idler emission could be obtained at much lower pump levels.

The idler output from the NOPA has a spectrum with more than one octave width extending from 750 to 1650 nm. It has an angular dispersion that fulfils a phase-matching condition among the pump, seed and idler with such a broad spectrum. The angular dispersion introduces difficulty in characterization of idler pulses with the bandwidth by using conventional up-conversion or down-conversion techniques. It makes it very difficult to achieve precise pulse compression. In order to overcome this difficulty in characterization, we employed cross-correlation frequency-resolved optical gating [53, 54] (XFROG) with broadband sum-frequency mixing (SFM). To attain the broad-enough-band in the SFM process, we applied the method of achromatic phase-matched SFM [55, 56] whose mechanism is similar to the one used to obtain a broader bandwidth for difference frequency amplification in NOPA [5] described in the previous subsection. In this way, we could utilize the full bandwidth of the idler with angular dispersion. In a cross-correlation method commonly used, only the delay-time dependence of signal intensity was measured and used for characterization. Hence it is difficult to characterize the pulse with shorter duration than the reference pulse width by this method, while the XFROG technique is able to characterize a pulse with shorter pulse duration than that of the reference pulse to be used. It is because the time–frequency contour map of the XFROG trace contains complete information, in principle, on the measured pulse. Compared with a SHG-FROG pulse diagnostics [57], the XFROG method has an advantage of the capability of obtaining more intense frequency-converted signals than the SHG-FROG by using an intense reference pulse. Furthermore, XFROG requires a narrower frequency-conversion bandwidth [58] than that needed in the SHG-FROG. This provides another advantage. Since the frequency-conversion bandwidth limits the thickness of the BBO crystal in both methods, a thicker crystal can be used in XFROG thanks to the narrower conversion bandwidth, resulting in possibly higher signal intensity. The XFROG measurement was performed with a broadband type-I SFM in a 30-μm-thick BBO crystal.

The above-mentioned two advantages enable the XFROG signal to be acquired with higher sensitivity than the SHG-FROG. The reference pulse was separately characterized by the use of an external SHG-FROG interferometer. An optical multichannel analyser (Ocean Optics S2000) was used to detect the XFROG signal. Taking advantage of the much narrower spectrum width of the reference than the measured pulse (idler) in the XFROG measurement, it is possible to

determine the group delay of the idler directly for each spectral pixel of the optical multi-channel analyser using the XFROG trace obtained without any retrieval. The centre of gravity of the delay time of the XFROG signal was defined as the group delay time at a wavelength corresponding to the data pixel. Then, the amount of the delay was fed back to each actuator of the corresponding wavelength in the deformable mirror. The Ti:sapphire fundamental radiation with the wavelength around 790 nm with about 120 fs duration, which is much longer than that of the reference pulse, was used for the XFROG.

The generated idler pulse was injected into the BBO crystal for the XFROG measurement after bouncing off the flexible mirror and transmission through a 2-mm-thick BK7 glass plate. The idler radiation of the NOPA was negatively chirped because the red part of the idler corresponds to the blue part of the positively chirped supercontinuum seed and vice versa. This negative chirp was coarsely compensated for by material dispersion of the BK7 glass, and the residual chirp was removed by a deformable-membrane (DM) mirror (OKO Technologies) with the adaptive control of 19 pixels. It is important to mention that it is impossible to introduce the positive chirp by the use of the BK7 glass in a spectral range longer than 1300 nm because of the anomalous dispersion of the glass material. However, the residual chirp after the BK7 glass was successfully compensated for by utilizing the DM mirror.

The Fourier-transform-limited (TL) pulse width was calculated from the retrieved spectrum to be 4.2 fs, which was close to the value calculated from the non-collinear OPA idler output spectrum. The retrieved pulse width from the XFROG measurement was 4.3 fs, which was close to the TL pulse width, so the chirp compensation, which corresponds to $\sim$1.3 optical cycles at a centre wavelength of 970 nm, worked successfully [46]. This result confirms that the broadband SFM-XFROG measurement was successfully performed with the full spectral bandwidth of the idler from the NOPA.

The part of the CEP-stabilized sub-5 fs pulse generation can be summarized in the following way. We have characterized broadband idler output pulses from a non-collinear OPA by using broadband SFM XFROG, taking advantage of the angular dispersion of the idler. By compensating for the residual higher order dispersion, using adaptive control of a deformable mirror, we achieved quasi-monocyclic NIR pulses with 4.3 fs pulse duration [46].

2.3. Compensation of angular and group-delay dispersions to generate a sub-3 fs pulse with CEP stability in the visible

As described in subsection 2.2, the idler output of CEP-stabilized NOPA had been compressed down to 4.3 fs. The idler output had a large angular chirp due to the non-collinearity of the beam configuration to satisfy the broadband momentum conservation in the parametric process. The angular chirp was considered to be an obstacle to characterize the pulse compression. However, this angular chirp problem was solved and further even utilized in the idler compression described in subsection 2.2. Adaptive group-delay tuning was made possible by using a DM in an ultra-broadband angular-dispersed SFM process, which was utilized for the XFROG
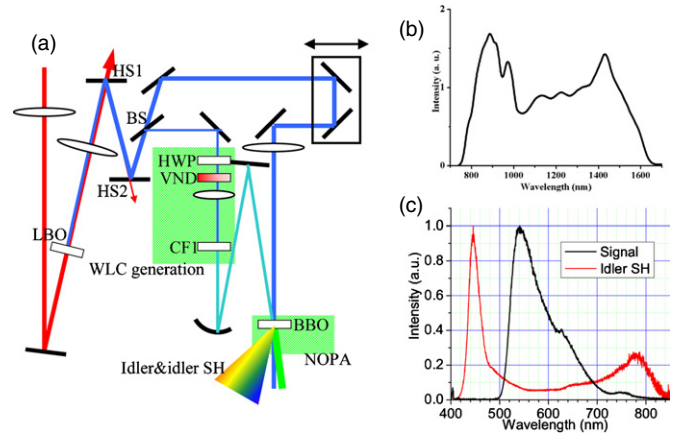

Figure 1. (a) Layout of NOPA (top view.) LBO: LiB_3O_5 crystal for second-harmonic generation. HS: harmonic separator. BS: beam splitter. HWP: half-wave plate. VND: variable neutral-density filter. CF1: calcium fluoride crystal fro white-continuum generation. BBO: β-BaB_2O_4 crystal for parametric amplification. (b) Spectrum of the idler pulse. (c) Spectra of idler-SH (solid black curve) and signal (broken red) [59].

measurement. Accidentally, the range of the exit angle of the idler with a chirp is substantially overlapping with the range of the phase-match angle for the type-I SHG of the idler in the NOPA BBO crystal. As a result, there was a considerable component of the SH radiation of idler (hereafter we call idler-SH) emitted from the NOPA BBO crystal. The spectrum of the idler-SH is extending in the range from 430 to 800 nm (figure 1(c)); hence its bandwidth is nearly twice that of the idler (figure 1(b)). It is natural to consider the compressed pulse duration of the idler-SH to be much shorter than that of the idler, 4.3 fs. It is also expected that the SH pulse of the CEP-stabilized idler pulse has a stable CEP which has two times of the constant phase of that of the idler. Therefore, even a shorter pulse with the stabilized CEP can be synthesized by combining electric fields of the idler and idler-SH even for the shorter CEP-stabilized pulse. To achieve this, both pulses should not have a large angular chirp; otherwise, the process of the spatial overlap of the two-pulsed beams for combination would be overly difficult. To avoid this problem, we tried to compress the idler-SH pulse with a near-zero angular chirp at the focal point of focusing optics. Pulse diagnosis was performed by the XFROG measurement [53, 54] with a collinear geometry. The pulse duration was measured to be 2.4 fs [59], which is the shortest ever reported in the visible–NIR range. We describe the details in the following.

The schematic of the CEP-stabilized NOPA system is shown in figure 1(a). The pump for the NOPA was the 400 nm pulse which was the SH of a Ti:sapphire regenerative amplifier (Spectra-Physics, Spitfire) with the repetition rate of 5 kHz. The pump energy was about 20 μJ, the pulse duration was about 70 fs and the radius of the focus spot at the surface of the NOPA crystal was about 50 μm. The NOPA crystal was a 1-mm-thick BBO crystal with the cut angle θ of 31°. The seed of NOPA was a supercontinuum light generated in a CaF_2 plate from the weaker (0.6 μJ) 400 nm light split out from the pump path. In this NOPA, the pump and the signal share the same CEP (because they are originated from the same SH
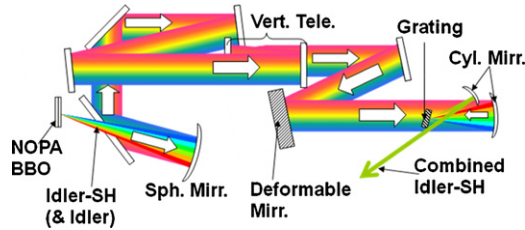
Figure 2. Schematic of the compensation system for angular dispersion and group-delay dispersion. Sph. Mirr.: concave spherical mirror for collimation. Vert. Tele.: telescope for reducing vertical beam width. Cyl. Mirr.: cylindrical mirrors for focusing onto the grating and collimating after the angular-dispersion compensation [59].

pulse). The experimental verification of the CEP stability of idler pulses was demonstrated by using spectral interferometry [60, 61]. This experiment was performed utilizing CEP-dependent optical poling with slow (about 1 s) feedback to suppress the CEP drift due to the cross-talk between the amplitude and phase in the parametric process.

The idler spectrum (figure 1(b)) spanned over more than one octave, with the wavelength range from about 770 nm to about 1.66 μm because the idler has substantial angular chirp (170 μrad nm^{-1}) to satisfy the phase-matching condition of NOPA. The angler dependence of the spectral on the idler pulse satisfies the condition of the phase matching for the angularly dispersed SHG [55, 62, 63] in the NOPA crystal. The SH of the idler (idler-SH) with the pulse energy of about 2 nJ was generated from the idler with about 500 nJ. The idler-SH radiation with horizontal polarization is spatially overlapping with the idler with vertical polarization. As described above, the idler-SH (figure 1(c)) has a quite broadband spectrum, spanning frequency width of broader than 300 THz. It had two pronounced peaks around 440 and 780 nm corresponding to the near zero angular mismatch for SHG.

The compensation of the angular dispersion and group-delay dispersion was accomplished with the optical setup as described in the following (figure 2). The concept of the setup was a hybrid of the Shirakawa and Kobayashi scheme [64] and the above-described idler compression to 4.3 fs by Adachi *et al* [46], used by our group before. It combined the angular dispersion compensation using a cylindrical mirror and a grating in the former and the adaptive group-delay dispersion compensation using a DM in the latter. Firstly, the idler-SH radiation emitted from the NOPA was diverging horizontally in a fan-like distribution and diverging slightly in the vertical direction due to the diffraction. It was collimated by a spherical concave mirror and thus its angular dispersion was converted into spatial dispersion. Then, to adjust the size of the beam to fit the size of the deformable mirror in the later stage the size in the vertical direction was slightly reduced with a vertical telescope composed of two concave mirrors with a small curvature difference. Then the rainbow-like spatially dispersed idler-SH was routed to a DM, which was composed of a membrane mirror driven by 19 linearly arrayed electrodes by electrostatic force. Because the idler-SH was spectrally dispersed on the DM surface, position-dependent deformation of the DM surface made it possible

to manipulate the wavelength-dependent group delay. Then the idler-SH was focused by a cylindrical concave mirror in the horizontal direction on the surface of a grating (1200 lines mm^{-1}), thus re-converting the spatial dispersion back to angular dispersion. Finally, diffraction by grating compensates the angular chirp, and the idler-SH was formed into a near-zero angular-chirp, whitish-coloured single beam.

The pulse diagnosis was performed with the SFM-XFROG method [53, 54]. The reference pulse used for the XFROG measurement was a 800 nm beam which was split out from the same Ti:sapphire regenerative amplifier output that is driving the NOPA. Because the original reference beam had large third-order dispersion, it was transmitted through a prism compressor. The reference pulse after compression was diagnosed with separate SHG-FROG [57] measurement and found to have the pulse duration of 45 fs.

The nonlinear material for SFM is a thin BBO crystal with the thickness of 10 μm. The wavelength-dependent phase mismatch and resultant reduction of SFM efficiency due to the broad spectral width of the idler-SH were evaluated theoretically and were compensated numerically after the SFM-XFROG measurement.

To avoid geometrical smearing and longitudinal walk-off between two corresponding beams, both of which will result in the temporal elongation of the XFROG signal, the idler-SH beam and 800 nm reference beam were incident to the BBO crystal collinearly. We used a chromium-coated partial mirror to overlap these two beams perfectly. The collinear geometry had some difficulties in detecting SF XFROG signal beam in the (near-) ultraviolet region (270–410 nm) as follows. Because the XFROG signal is generated in the same direction as idler-SH and 800 nm reference beams, there are three problems. Firstly, reference beam saturates the spectrometer (Ocean Optics USB4000) used for detecting the XFROG signal. Secondly, scattering of the idler-SH in the spectrometer generates a large background noise in the detected signal. Thirdly, there is also relatively strong SH of the reference beam with the wavelength around 400 nm.

These problems were solved in three steps. Firstly, we filtered out idler-SH and 800 nm reference by a Gran-Thompson prism, utilizing the polarization difference. Secondly, we set up a spectral filter using the dispersion of quartz prism and removed the leakage of 800 nm reference through the Gran-Thompson prism. Thirdly, we subtracted the signal due to the SH of the reference beam as the background, which was always present regardless of the delay of reference.

The XFROG trace taken just before the adaptive group-delay dispersion compensation process described later in the text is shown in figure 3. The group-delay dispersion compensation process using DM was made in two steps. The first process is the pre-measurement of dependence of the group delay upon the DM electrode voltage change, and the second process is to minimize the group-delay variation over the entire spectrum by the negative feedback loop using the following pre-measurement result.

We performed two types of pre-measurements. Firstly, we investigated the relationship of one-electrode voltage change to group-delay change. Whereas the voltages supplied to
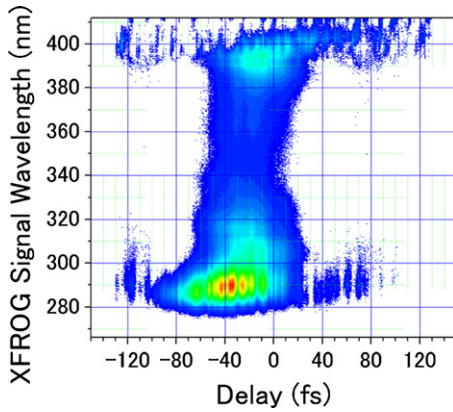
J. Phys. B: At. Mol. Opt. Phys. **45** (2012) 074005

T Kobayashi *et al*

Figure 3. SFG-XFROG trace before deformable-mirror adjustment.

Figure 4. Group-delay changes by the changes of deformable-mirror tenth electrode voltage. Flat line at zero: '0' voltage curve. Solid black curve: '64 voltage curve'. Dotted red: '127' voltage curve. Broken green curve: '196' voltage curve. Solid blue curve: '255' voltage curve. Only relative changes from the '0' voltage case are shown and vertical position of traces are adjusted by adding an arbitrary constant group delay to make the changes caused by the voltage change clearly separated.

the 19 DM electrodes of the deformable mirror could be set independently as positive integers from 0 to 255, all electrode voltages other than the tenth electrode were set at '180'. Of course, there is no specificity of the tenth electrode, and it is also possible to use another electrode as the standard electrode in the following process. Then, the tenth electrode voltage was set at five different values '0', '64', '127', '196', '255' and five different group-delay spectra were taken for each voltage setting.

In the same way as described in subsection 2.2, if a clean reference pulse with a significantly narrow bandwidth is compared with the signal diagnosed (in this case, idler-SH) in the SFM-XFROG measurement, then the group delay of the signal at a particular wavelength can be crudely estimated by the delay of the peak of the SFM-XFROG signal at the corresponding wavelength. Therefore, we tracked the peak of SFM-XFROG traces in the wavelength direction and estimated group-delay spectra without performing time-consuming XFROG retrievals. We used this method for temporal characterization throughout the entire group-delay dispersion compensation process.

The five different group-delay spectra taken for the five different electrode voltages are shown in figure 4. Note that only group-delay differences compared with voltage '0' are shown and the '0' case is pure zero throughout the entire wavelength range. From the measured group-delay changes, they are found to be proportional to the square of the electrode voltage as expected.

Secondly, we measured the wavelength dependence of the group-delay change for each DM electrode. Voltages of all of the DM electrodes were set to '180' except for the electrode of interest. The electrode of interest was driven to '255', and the XFROG trace was measured and the estimated group-delay spectrum obtained by the measurement was compared with the '180' case. The 19 curves corresponding to each 19 electrodes are shown in figure 5.

The minimization of the group-delay variation over the spectral components by the negative feedback loop was preceded in the following three steps. In the first step, we measured the XFROG trace and calculated the group-delay spectrum with the current DM setting (for the very beginning, all were '180').
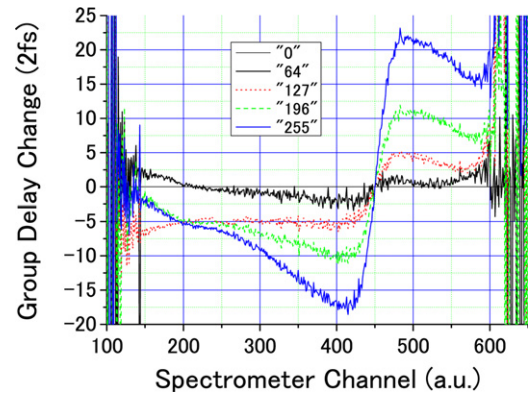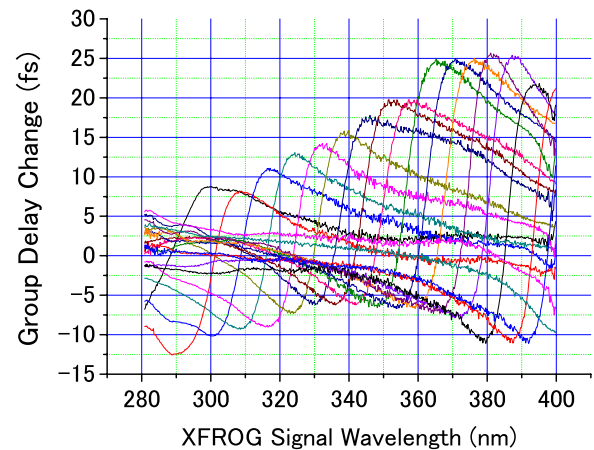

Figure 5. The 19 cases of group-delay changes by the application of '255' voltage to each electrode. Each curve shows the case when '255' voltage was applied to only one particular electrode out of the 19 electrodes and all other electrodes were set to '180'. Only relative changes from the '180' voltage case are shown.

In the second step, we calculated the DM electrode voltages which would cancel the group-delay variation measured in the first step. In the calculation, the effect of the voltage of each electrode upon the group-delay spectrum is assumed to be independent (i.e. no nonlinear interaction between electrodes). The effect of an electrode is assumed to be proportional to the result of second step pre-measurement, and to be scaled with the square of each electrode voltages. The assumption of non-nonlinear interactions, the combined effect of displacement of all pixels connected to corresponding electrodes, is simply the sum of the displacement induced by each electrode. The assumption of linear scalability may be considered to be too simple, but because the calculations were in the negative feedback loop, the errors due to the assumption would also be minimized in the process.
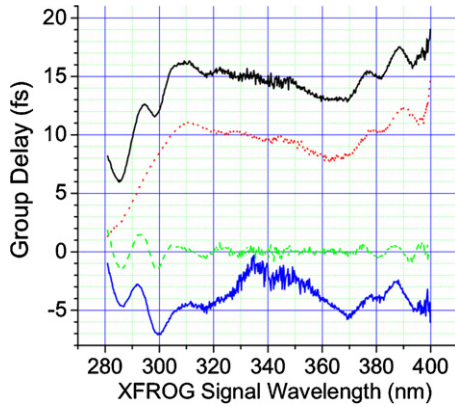
Figure 6. Group-delay spectra for one deformable-mirror feedback cycle. Shown in order from top to bottom. Solid black curve: observed initial group delay. Dotted red: simulated group-delay change caused by the application of updated electrode voltages. Broken green: simulated residual group delay after the update of electrode voltages. Solid blue: observed group delay after the actual update of electrode voltages. Arbitrary constant group delay was added to each curve.

In the final step, we applied the voltages calculated in the second step to the actual DM electrodes.

Then, we returned to the first step, and if group-delay variation (or the change of it) was small enough, stopped the feedback loop and proceeded to XFROG retrieval. The loop was executed manually (calculations were performed using Octave, a MATLAB clone), taking 1 to 2 h for each loop.

An example of change in the group-delay spectra at each feedback cycle is shown in figure 6. The calculated group-delay change in the second step mimicked the measured group delay quite well, and the residual group delay predicted as the after-one-loop result contained only small variation. But actual group-delay measurement after the application of the calculated DM voltages revealed non-negligible group-delay variation. Nonetheless, the negative feedback loop was effective as a whole, and substantial reduction of group-delay variation was observed. The group-delay variations throughout four iterations of the negative feedback loop are shown in figure 7. Since the improvement after the fourth iteration from the third one was found to be marginal, we concluded this is the final step of the minimization of the group-delay dispersion and proceeded to the XFROG retrieval.
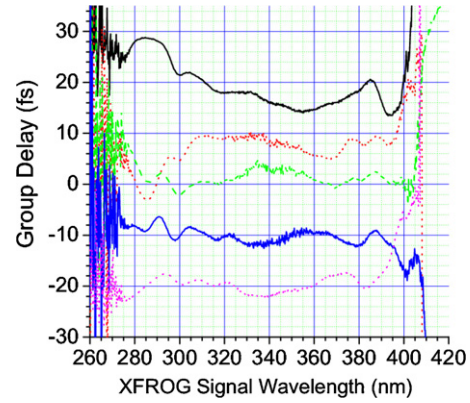

Figure 7. Group-delay variation reductions throughout the four cycles of negative feedback loop. Shown in order from top to bottom. Solid black curve: initial (0th) group delay. Dotted red: after first feedback. Broken green: second. Solid blue: third. Dotted pink: fourth (last.) Arbitrary constant group delay was added to each curve.

The measured and the retrieved XFROG traces are shown in figure 8. They match well and the FROG error for the retrieval was 0.0157. The temporal shape of the idler-SH retrieved is shown in figure 9(a). The pulse duration is 2.4 fs, well below 3 fs. Although there are relatively strong satellites on both sides of the main pulse, the energy contained in the main pulse was about 47%, nearly half of the total pulse energy of about 1 nJ. The Fourier-transformation-limited pulse duration calculated from the spectrum was 2.2 fs, so the achieved pulse was close to transform limited. The spectrum of idler-SH retrieved is shown in figure 9(b) and it coincides well with the spectrum of idler-SH directly measured using the spectrometer.

The substantially high intensities of satellites and the relatively low intensity of both of the centre wavelength in the spectral shapes might be both due to the leftover angular dispersion in the idler-SH. With the tuning of the group delay using DM, the angular dispersion, originally adjusted to near zero, was slightly increased. In order to solve this problem, the introduction of negative-chirped mirrors and pair of fused-silica wedges to give a variable positive chirp and the reduction of DM drive are considered to be feasible.

In summary, we have achieved sub-3 fs pulse duration in the visible and NIR regions by compressing the SH of CEP-stabilized NOPA output (idler-SH.) The spectrum of the
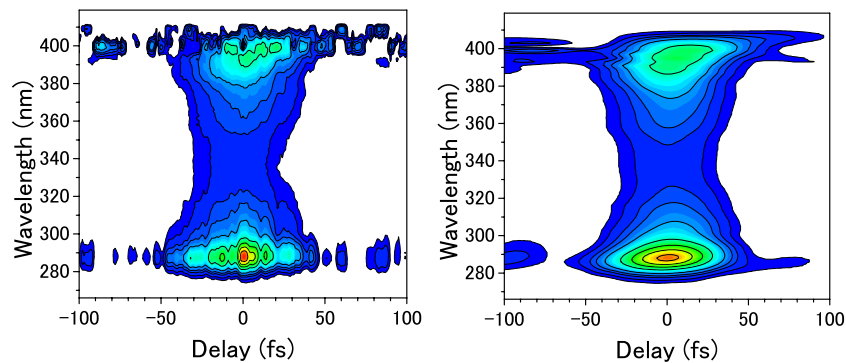

Figure 8. (a) SFG-XFROG trace of idler-SH. (b) Retrieved trace from (a) [59].
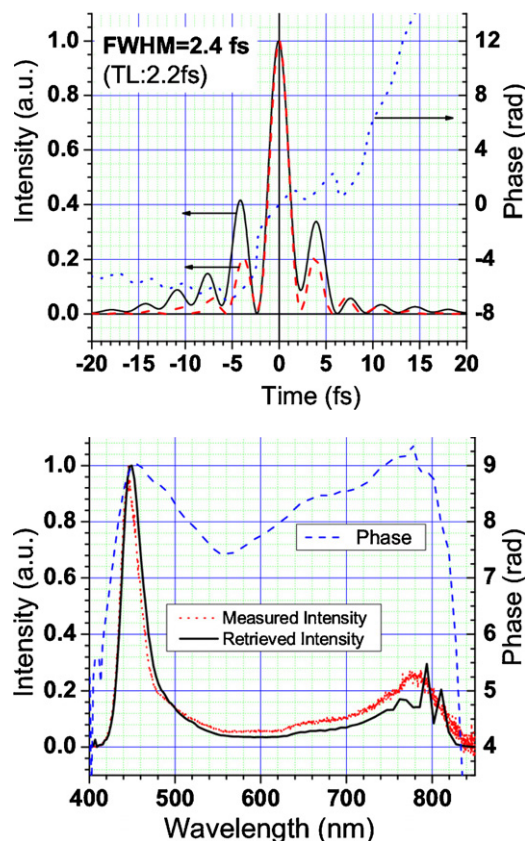
Figure 9. (a) Retrieved temporal pulse shape. Solid black curve: retrieved intensity. Dotted blue curve: retrieved phase. Broken red curve: intensity of the TL pulse. (b) Retrieved and measured spectral pulse shape. Solid black curve: retrieved intensity. Dotted red curve: measured intensity. Broken blue curve: retrieved phase [59].

pulse is smooth and considered to be suitable for spectroscopic applications. For a pump–probe experiment, the energy of idler-SH is too low to be used as the pump beam, but the NOPA used also emits the energetic (nearly 1 μJ) signal beam, which can be used as the pump beam. From its bandwidth, the signal beam is considered to be compressible down to 6 fs.

The method using the signal as the pump and idler-SH as the probe has a novel advantage thanks to the different CEPs between them. The CEP of the signal fluctuates according to that of the Ti:sapphire regenerative amplifier, whose output fluctuates. This fact means that the phase of interference fringe between the signal and idler-SH differs shot by shot. Thus, when averaged for about a second, i.e. several thousand shots, the interference feature will be washed out and will not contaminate the difference-absorption (DA) signal. This is in stark contrast with the usual case of common-CEP pump and probe (split into two from one beam), in which the interference overrides the DA signal near the zero delay.

As a prospect, there is a possibility of even shorter pulses being generated with the linear superposition of idler-SH and idler radiation. Because they are synchronized (same origin), have constant CEP, cover wavelength range next to each other and compressible independently down to near-TL pulses, sub-2 fs pulse synthesis may be possible by this method (the synthesized pulse would cover the range of 420 nm to 1.6 μm). Although such ultimately short pulses in the visible

and NIR will be quite difficult to handle under the atmospheric condition, they will be an invaluable tool for investigating molecular dynamics or chemical reaction processes observing an extremely broad spectroscopic range from a single source.

3. Pulse shortening and sub-femtosecond pulses generation using CFWM

In past years, Raman scattering that relied on molecular modulation driven in gaseous molecules by two independent nanosecond lasers offers an attractive alternative to HHG for sub-fs pulse generation owing to its high conversion efficiency [30]. In this technique, multicolour narrow Raman sidebands separated by the frequency difference between the two driving lasers are spatially dispersed by a prism and phase controlled by liquid–crystal modulator [28]. Due to the narrow band of the sidebands, a single isolated sub-fs pulse cannot be generated, and it is difficult to isolate a single pulse from the obtained pulse train composed of pulses with nearly equal intensity.

By using two crossing beams of femtosecond pulses, a similar cascaded Raman scattering phenomenon was found in many solid-state materials, such as $PbWO_4$ [65, 66], TiO_2 [67], $LiNbO_3$ [68], $KNbO_3$ [69], $SrTiO_3$ [70], $KTaO_3$ [71, 72], $YFeO_3$ [73], diamond [74] and BBO [75]. More than 20 coherent sidebands were recently generated by focusing two-colour ultrashort pulses into a Raman-active crystal, such as lead tungstate ($PbWO_4$) and diamond [65, 65, 74]. By combination and dispersive compensation of several sidebands generated in $KTaO_3$, a 10 fs single pulse has been obtained [72]. Another mechanism of multicolour-sideband generation is CFWM in an isotropic transparent bulk medium. There is a difference in tunability between this method and the Raman method. The sidebands by CFWM can be tuned by rotation of the nonlinear plate, while those from Raman process are fixed. The CFWM process was experimentally studied in a BK7 glass plate in 2000 for the first time [76]. Recently, Weigand *et al* further demonstrated coherent spectra spanning over two octaves in the visible and ultraviolet ranges using a 150 μm fused-silica plate, which supports a visible-UV spectral band broad enough to generate near-single-cycle 2.2 fs pulses without recurring to complex amplitude or phase control [77, 78]. In the process, the wavelength of the generated multicoloured sidebands is tunable by changing the crossing angle between the two input beams [79–82]. From the results and theoretical expectation using the scaling, it is expected to be possible to obtain a sub-fs pulse with 400 nm and the shifted spectrum from the 400 nm by SPM as two incident pulses for CFWM in BBO crystal or diamond to obtain a multicolour UV pulse which can be compressed to 0.8–0.9 fs. It is also interesting to generate such multicolour UV pulses in several hundred (400–500) attosecond using the fs pulse in the spectral range of 260–270 nm and another pulse spectrally shifted by SPM as two incident pulses for CFWM in solid Xe or Ar.

Ultrashort DUV to UV pulses are very important to study the excited state's very basic molecules such as methane and benzene and biologically important molecules such as amino acids. Also far UV(FUV) extending from 200 to 120 nm, corresponding to 6.2 to 10.2 eV, is useful to study
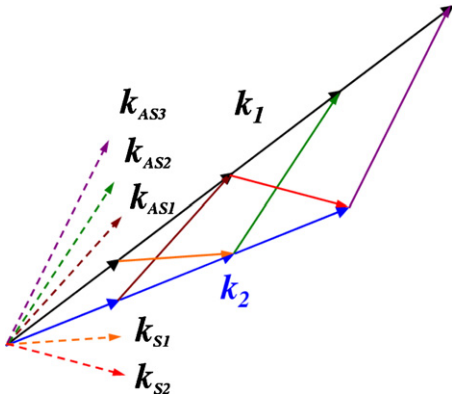
J. Phys. B: At. Mol. Opt. Phys. **45** (2012) 074005

T Kobayashi *et al*

Figure 10. Phase-matching geometry for the CFWM process. k_1 and k_2 are the wave vectors of two input beams. S_m and AS_m are the generated mth order down-shifted and up-shifted sidebands, respectively [83].

Figure 11. Schematic of the experimental setup. Filter: BPF at 700 nm centre wavelength with 40 nm bandwidth, or SPF with cut-off wavelength at 800 nm. Delay: delay stage. Bulk media: solid plate such as CaF2, fused-silica, sapphire plate, or BBO crystal.

the mechanism of the origin of life, namely the production of amino acid from CO_2, NH_3, N_2, and H_2O by DUV-FUV excitation, which may have taken place in the early Earth. In the early Earth lacking O_2 and ozone (O_3), intense UV was irradiating on our Earth to introduce such reactions driving the reactions to generate such molecular components. It is of vital importance to study such chemical reactions relevant to the mystery of the origin of life. Using ultrashort UV-FUV pulses with several hundred attoseconds prepared by the above-mentioned methods may enable us to reveal such an important subject. This can also make it possible to understand the UV damaging processes in amino acid and DNAs which induces cancer. This problem is becoming more and more important under the problem of the situation of the Earth with ozone holes in this century.

Furthermore, the sub-fs pulse extending to the UV, DUV and FUV range is useful for the study of various chemical reactions in general. It is expected to reveal the transition states and intermediates in the reaction process to visualize the molecular structural change during the reaction triggered by such short pulses. Since varieties of materials are generated via chemical reactions of molecules and biological processes, in which *outmost electrons* are playing the most important role. This is in contrast to the research field realized by the application of sub-100 attosecond pulses in the range of XUV and soft x-ray. The sub-100 attosecond pulse is well known to be useful to study the dynamics of the electronic wavepacket of *inner-shell electron*s instead of outmost electrons.

Single sideband with pulse duration as short as 15 fs has been generated using CFWM with chirped incident pulses in a 1 mm thick fused-silica glass [82]. Then, it is applicable to obtain a sub-fs pulse by using a transparent solid bulk medium as the nonlinear medium to generate Raman sidebands or CFWM sidebands when the two incident pulses are CEP stable.

CFWM is explained schematically in figure 10. In the process, each step of sideband generation is a four-wave mixing process. Then the phase matching is needed to be satisfied in every cascading step, as shown by the following equations [83]:

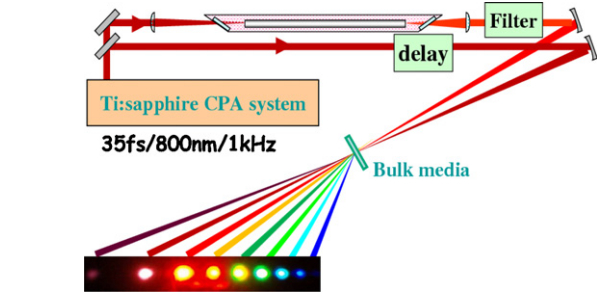$$k_{AS_m} = k_{AS_{(m-1)}} + k_1^{(m)} - k_2^{(m)} = (m+1)k_1^{(1)} - mk_2^{(1)}, \quad (3a)$$

$$\omega_{AS_m} = (m+1)\omega_1^{(1)} - m\omega_2^{(1)} \quad (3b)$$

$$k_{S_m} = k_{S_{(m-1)}} + k_2^{(-m)} - k_1^{(-m)} = (m+1)k_2^{(-1)} - mk_1^{(-1)}, \quad (4a)$$

$$\omega_{S_m} = (m+1)\omega_2^{(-1)} - m\omega_1^{(-1)}. \quad (4b)$$

Here, k_1 and k_2 are the wave vectors of the two input beams with respective frequencies of ω_1, ω_2 ($\omega_1 > \omega_2$), integer m is the generated order of the sidebands, and AS_m and S_m are the mth-order spectral upshifted and downshifted sidebands, respectively. Equations (3a) and (4a) are the phase-matching conditions corresponding to the momentum conservation relations and (3b) and (4b) are the energy conservation relations among the involved photons.

The schematic of the experimental setup is shown in figure 11. The experiments were performed using a 1 kHz Ti:sapphire regenerative amplifier laser system (Micra + Legend–USP, Coherent). The system generates 35 fs pulses of about 2.5 mJ per pulse at a repetition rate of 1 kHz with the central wavelength at 800 nm. About a 300 μJ beam (called beam 1, k_1) was focused into a hollow-core-fused-silica fibre to obtain a broadband spectrum. A spectral filter (BPF1: band-pass filter (BPF) at 700 nm centre wavelength with 40 nm bandwidth) was used to filter out the wanted spectrum. After a delay stage, beam 2 (k_2) was first optimally attenuated by a variable neutral density (VND) filter and it was then focused into the transparent bulk medium together with beam 1.

When a 1-mm-thick fused silica was used as the nonlinear medium, as many as 15 anti-Stokes signals and two Stokes signals were obtained [79]. The spectra are extending from 320 nm to 1.2 μm with more than 1.8 octaves. Even though the pulse energy of the high-order anti-Stokes was low, the broadband spectrum is still of great interest. These broad distributed sidebands can be used to obtain a near single-cycle pulse with strong satellite pulses through Fourier synthesis of the sidebands [77, 78]. When the intensities of incident beams are increased to a high enough level, four-wave optical parametric amplification and cross-phase modulation processes also broadened the spectrum and amplified the energy of every sideband [84]. Then, the separated spectrum of every sideband becomes a single broadband with a nearly continuous spectrum without clear gaps between all of the neighbouring peaks only with small modulations between them. Figure 12 shows the spectra of the beams of the
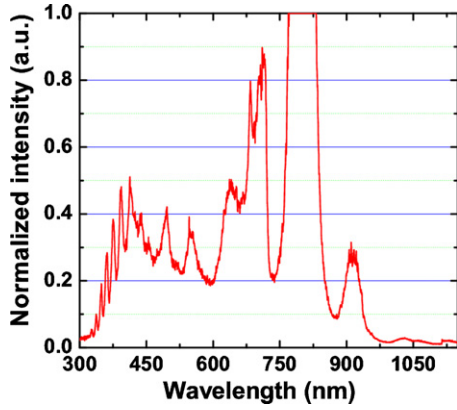
Figure 12. Spectrum of the scattering light of the generated sidebands collected from a white sheet of paper 15 cm apart from the glass plate and measured by a USB4000 spectrometer.

sidebands and the two incident pulses projected to a white sheet of paper. This spectrum is normalized to be constant, so it does not reflect the actual intensity distribution of the sideband components. However, intensity distribution can easily be modified to be nearly constant by utilizing an appropriate filter. The transform-limited pulse duration of the spectrum is calculated to be about 1.2 fs with a quasi-single pulse structure without any substantially intense satellite pulses. This work is ongoing in our laboratory now.

Besides the range of the whole spectrum of the multicoloured pulses, the centre wavelength of each sideband can be tuned by changing the crossing angle of the two incident beams [81]. The negative chirp or self-compressed multicoloured sideband pulses can be obtained with two oppositely chirped incident pulses [82, 83]. Figure 13 shows the multicoloured sidebands obtained by using a 1-mm-thick fused-silica glass as a nonlinear material. The spectra of AS2 can be easily tuned by simply changing the crossing angle between the two incident beams. Figure 14 shows the retrieved pulse profile and temporal phase of the AS1 and AS2 pulses which indicates a small negative chirp in the pulse. The retrieved pulse duration is 15 fs for AS1 which is expected to be sub-10 fs when the negative chirp was completely compensated. The spectral phase of AS2 is nearly constant except for some high-order dispersion. The pulse duration is 16 fs for AS2 which is close to the transform-limited pulse duration of 12 fs. Both AS1 and AS2 own much shorter pulse duration than that of the incident pulses and even shorter than the transform-limited pulse duration of the incident pulses. These properties also make them useful in the multicoloured pump–probe spectroscopy and some other applications to utilize the multiplicity of the colour.

The CFWM process was also observed in many other bulk media such as a sapphire plate [81] and CaF$_2$ crystal [82]. Two-dimensional multicolour sideband was also obtained in a sapphire plate [81, 83, 85]. To extend the phase-matching bandwidth and obtain more components of multicolour sidebands, thinner material with low dispersion should be used as the nonlinear medium. However, the use of a thinner glass plate will reduce the CFWM efficiency. Then, material with a high damage threshold is useful to increase the incident pulse

intensity resulting in the increase in efficiency. This work is now ongoing.

Figure 13(a) shows the spectra of AS1–AS5 and S1 which are very clean and smooth without any structure, while incident beam 1 has some shoulder. The M^2 of AS1 was measured to be 1.01 and 1.06 in the horizontal and vertical directions, respectively [83]. Even when the incident pulses of beam 1 and beam 2 have relatively complex spiky structures [79–82], the spectra of the CFWM beams are very smooth and featureless. In this way the generated signals by the CFWM processes have high-quality properties in both frequency and wave vector spaces. The mechanism of this cleaning process can be explained as follows.

The spectra of the signals can be calculated with equations (3*a*) and (4*a*) based on the phase-matching condition. Although it can qualitatively explain the main spectral components of the signals, the spectral shapes cannot be obtained by the simple equations. The analysis should begin with an integral description of the FWM nonlinear polarization density. The third-order dielectric polarization induced at frequency Ω by the input beams can be expressed by summing over all possible permutations of the input frequencies according to the third-order susceptibility

$$\tilde{P}^{(3)}(z, \Omega) = \iint d\omega_1 \, d\omega_2 \, \tilde{\chi}^{(3)}(\Omega : -\omega_1, \omega_2, \Omega + \omega_1 - \omega_2)$$
$$\times \tilde{E}_1^*(z, \omega_1)\tilde{E}_2(z, \omega_2)\tilde{E}_3(z, \Omega + \omega_1 - \omega_2) \exp[i(-k_{1z}(\omega_1)$$
$$+ k_{2z}(\omega_2) + k_{3z}(\Omega + \omega_1 - \omega_2))z]. \tag{5}$$

Double integration in equation (5) is performed over ω_1 and ω_2 with the integrand being the product of amplitudes of fields 1, 2 and 3 and the third-order susceptibility. In the case of present CFWM, it is considered that the conditions of ω_1, $\omega_2 > \omega_3$, $\omega_1 \sim \omega_2$ are satisfied, and the equation represents the polarization source term of AS signals. In the above expression, we assume that the pulses are nearly Fourier limited and overlap each other well over time. These conditions are needed for the pulses overlap during the entire time of interaction to produce a signal with the same spectral components. Representation of the frequency-dependent third-order nonlinear susceptibility $\tilde{\chi}^{(3)}(\Omega : -\omega_1, \omega_2, \Omega + \omega_1 - \omega_2)$ is based on the interaction of the input fields with an electronic transition with the frequency ω_{eg}. In the case of a nonlinear process with a low efficiency ($E_{1,2,3} = \text{const}$), the four-wave mixing signal field can be obtained through integration of the signal intensity over the longitudinal coordinate z.

As a result, the spectral intensity of the generated FWM signal is an integral of the product of the spectral intensity of two incident laser fields in a FWM process as shown in equation (5). The intensity of the generated FWM signal can be given as

$$I_{FWM}(\omega_{FWM}) \propto \left| \iint d\omega_1 \, d\omega_2 \, \chi^{(3)} E_1^*(z, \omega_1) E_2(z, \omega_2) \right.$$
$$\left. \times E_1(z, \omega_{FWM} - \omega_2 + \omega_1) \sin c(\Delta k_z(\omega_{FWM}, \omega_1, \omega_2)L/2) \right|^2. \tag{6}$$

Here, ω_{FWM} and ω_1 and ω_2 are the angular frequencies of the generated FWM signal, and the two incident beams,
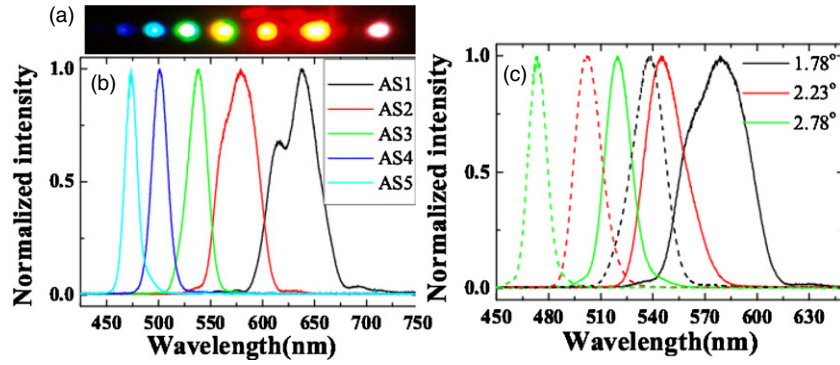
Figure 13. Photograph of the sidebands on a sheet of white paper placed 30 cm behind the glass plate when the crossing angle between the two input beams is 1.78°. The first, second and third spots from the right-hand edge are beam 2, beam 1 and AS1, respectively. (b) Spectra of the sidebands from AS1 through AS5 when the crossing angle between the two input beams is 1.78°. (c) Spectra of AS2 and AS3 with the crossing angles of 1.78°, 2.23° and 2.78° [82].
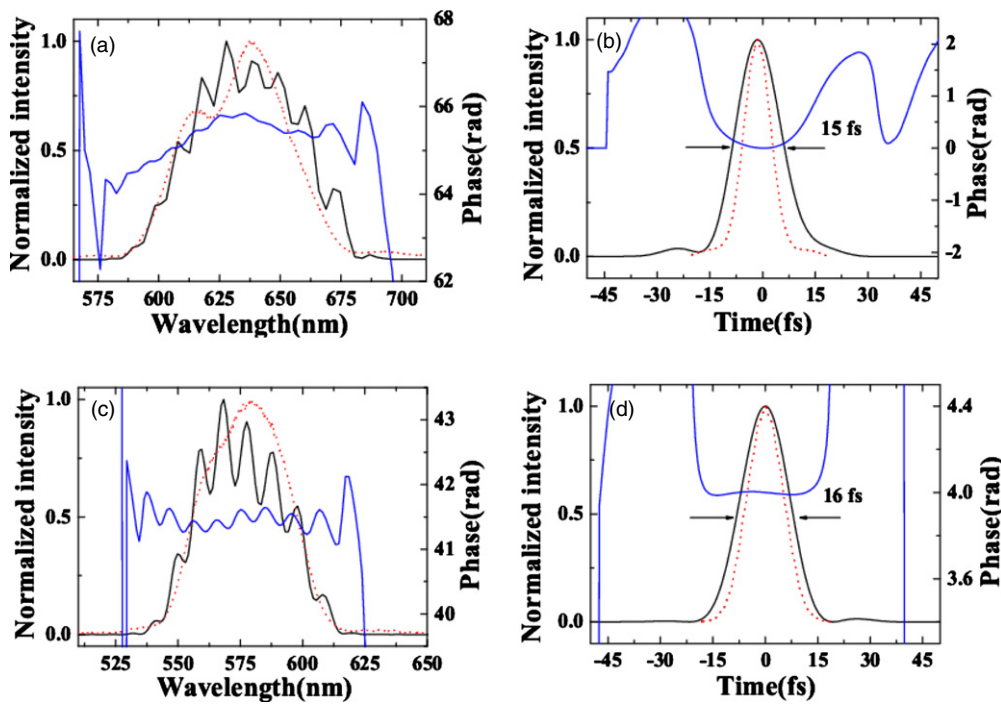

Figure 14. (a) Recovered spectrum (black solid curve), spectral phase (blue solid curve) and measured spectrum (red dotted curve) of AS1.
(b) Recovered intensity profile and phase of AS1. The red dotted curve shows the transform-limited (FWHM = 9 fs) pulse profile of AS1.
(c) Recovered spectrum (black solid curve), spectral phase (blue solid curve) and measured spectrum (red dotted curve) of AS2.
(d) Recovered pulse profile and phase of AS2. The red dotted curve is the transform-limited (FWHM = 12 fs) pulse profile of AS1 [82].

respectively. $\Delta k_z(\omega_{\mathrm{FWM}}, \omega_1, \omega_2)$ is the phase mismatch and L is the path length in the medium. The expression means that the intensity of the generated FWM signal at every wavelength component is an averaged contribution over the whole spectral region of the incident pulses. Therefore, the spectrum of the generated FWM signal is smoothed automatically even though the spectra of the incident pulse contain complex structures. The spectral phase of the generated FWM signal is also smoothed in the same way. Moreover, this averaged contribution makes the central wavelength components be suppressed and the weak wings on both sides be enhanced. Simultaneously, from the phase-matching condition, a new wavelength will be generated on both sides of the generated

FWM signal spectrum. As a result, the spectrum of the generated FWM signal is broadened.

In the time domain, the generated new signal can be simply expressed as $I_{\mathrm{FWM}} \propto I_1^2(t)I_2(t-\tau)$. This expression indicates that the generated new signal has shorter pulse duration and a much higher temporal contrast than that of the two incident pulses. These results are consistent with the results in the frequency domain.

As discussed above high-quality multicolour pulses can be obtained by *utilizing the limitation imposed by the phase-matching* condition. This is a high contrast to the application of non-collinear configuration for the *relaxation of the phase-matching* condition to generate an ultrashort pulse in NOPA. In the latter process, instead of eliminating the limitation as an

obstacle, the phase-matching condition is positively utilized in the former process.

There is also another contrast between the CEP stabilization and contrast enhancement. The former is attained by the *subtraction* process of the phases in the nonlinear process. In the case of the CFWM, integration (*addition*) over the spectral component reduces the spiky fine structure to obtain a smooth spectrum.

4. Novel generation method for a simultaneously cleaned and compressed pulse to be applied to intense attosecond pulse generation

Due to the low-conversion efficiency and low-intensity threshold of ionization of the medium, the energy of isolated attosecond pulses is limited to the sub-nanojoule or nanojoule range by HHG in gases [86, 87]. To obtain intense attosecond pulses for developing their applications, an alternative efficient method is to use solid targets as a nonlinear medium for HHG. The coherent wake emission (CWE) [88] and the oscillation of the plasma surface at relativistic velocities [89] are the two different mechanisms for intense HHG in a solid target. Many experimental results have shown that laser pulses with high temporal contrast are important to prevent the unwanted intense prepulses which can generate preplasma before the main pulse arrives at the target [31].

Recent experiments of the generation of the attosecond pulse or high-energy particle showed that the excitation pulse with a higher temporal contrast by some cleaning mechanism will improve the stability and efficiency of the generated attosecond pulse or a high-energy particle [90]. Among many techniques for pulse cleaning, the third-order nonlinear process, especially for cross-polarized wave (XPW) generation, has recently become popular because of higher improvement in contrast than others [91–94]. In the third-order nonlinear process, utilizing non-resonant electronic nonlinearity free form inertia, the generated signal can be expressed simply as $I_{SD1} \propto I_1^2(t)I_{-1}(t-\tau)$ for two pulses with the temporal intensity distribution of $I_1(t)$, and $I_{-1}(t)$ with the delay time of τ. This means that the temporal contrast of the generated signal can be estimated as the cube of the temporal contrast of incident pulses when the split beam of the common pulse is used. In a non-resonant electronic Kerr medium, the third-order nonlinear process is an instantaneous process with femtosecond timescale because of inertia-free interaction [95]. Then, the weak amplified spontaneous emission (ASE) and satellite noises will have separated nonlinear processes in time from the main pulse and pulse can be cleaned even in the picosecond range.

SD is also another third-order nonlinear process and can be used for the enhancement of intensity ratio between main pulse and satellite and/or pedestal. SD is a degenerated four-wave mixing process. It must satisfy the phase-matching condition.

Usually, the phase-matching bandwidth of different parameters is defined as the phase mismatch Δk satisfies the condition that the amount of phase shift between the diffracted signal and the incident, $|\Delta k| L$, accumulated during the propagation of them over the thickness of the medium, L,
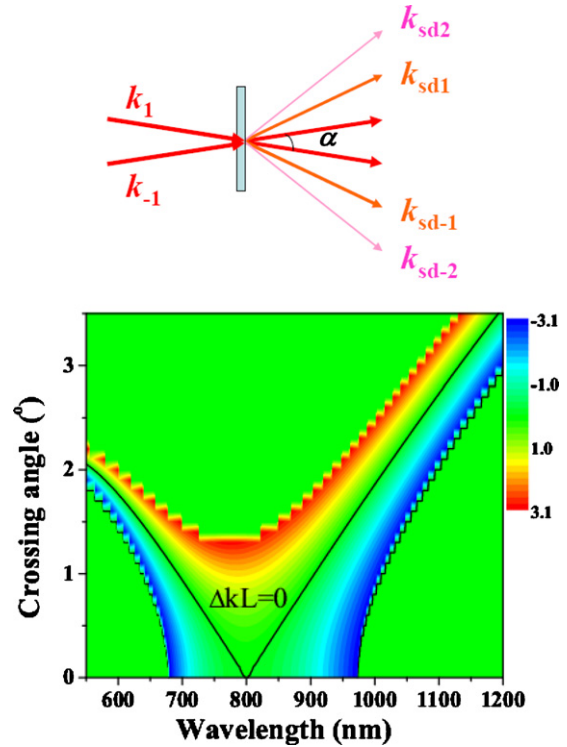

Figure 15. Top: experimental geometry for the SD process. α is the incident crossing angle. k_1 and k_{-1} are wave vectors of the two incident beams and k_{sd1} and k_{sd-1}, k_{sd2}, k_{sd-2} are wave vectors of the two generated first- and second-order SD signals. Bottom: two-dimensional phase-mismatch distribution plotted against the crossing angle and the probe wavelength when the pump wavelength is fixed at 800 nm. The black solid curve shows the condition satisfying the zero phase mismatch.

is smaller than π. The phase mismatch was calculated with the wavelength of the pump beam being fixed at 800 nm. The phase mismatch $|\Delta k| L$, dependent both on the crossing angle and the central wavelength of the other incident beam, is calculated. Figure 15 shows the two-dimensional pattern that the phase mismatching changes with the crossing angle and with the probe wavelength in a 0.5-mm-thick fused-silica glass plate. It can be seen that the phase-matching spectral range is broader than 300 nm when the crossing angle is around $1°$. Then phase-matched spectral range can be extended to more than one octave when a thinner glass plate is used.

The experimental geometry is shown in figure 15. The laser is from a commercial Ti:sapphire CPA laser system with 35 fs at 800 nm centre wavelength. The two beams beam_1 and beam_–1 with the wave vectors of k_1 and k_{-1}, respectively, were focused by a spherical mirror with a 300 mm focal length into a 0.5-mm-thick fused-silica glass plate located about 20 mm after the focal point. The beam diameters on the glass plate were both about 360 μm at the intensity of $1/e^2$ on the peak. The crossing angle (α) between the two incident laser beams was about $1.5°$. Then, the phase-matching condition can be easily satisfied as shown in figure 15. The individual transmission pulse energies after the glass plate were 40 and 51 μJ, respectively. SD signals appeared on both sides besides the input beams when the two beams were temporally synchronized and spatially overlapped on the glass
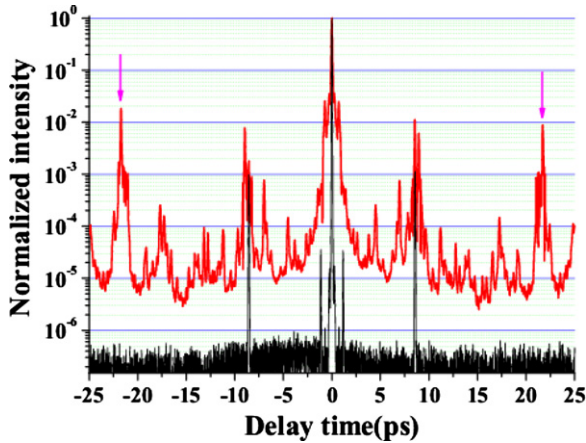
Figure 16. (a) SF intensities of the incident pulse (upper red curve) and of the SD1 signal in the delay time from –25 to 25 ps and with a 10 fs per step resolution [97].

plate. The pulse energies of the generated first-order SD (SD1) signals were about 5 and 6 μJ besides beam_1 and beam_–1, respectively. The energy efficiency of frequency conversion from the input laser beams to two SD1 signals was about 12%.

Due to the low pulse energy and the low power level of the generated SD signals, we performed a SHG-FROG, which requires only much lower incident pulse energy and is more sensitive to the low-energy noise than the third-order autocorrellator, since it involves only one second-order nonlinearity, to obtain the information of the pulse contrast [96]. A 70-μm-thick BBO (Type I, $\theta = 29.2°$) crystal was used to generate the SF signal with one arm scanned with a 10 fs per step. After passing through an aperture, a short-wavelength-pass filter cutting at 440 nm, and a neutral-density (ND) filter reducing by 1/1000 times, the SF signal was focused into a fibre and detected by a multi-channel spectrometer (USB4000, Ocean Optics) with 100 ms integration time. Figure 16 shows the intensities of the SF signals of the incident pulse and the SD1 pulse from –25 to 25 ps.

In comparison with incident pulses, it is very clear that the temporal contrast of the SD1 signal is improved by about 4.5 orders of magnitudes. Even in the time range of ± 0.7 ps apart from the main pulse peak, the SF peak intensity is about

1.2×10^{-2} of the main pulse for the incident pulse. The SF intensity of the SD1 signal shows that there is a small peak at the same delay time with less than 1.2×10^{-6} of the peak intensity of the main pulse. This indicates that even better than the calculated improvement of 1.7×10^{-6} is expected from the calculation using the cube of 1.2×10^{-2}. Other than the improvement due to the SD process, the self-focusing process and the pulse compression also help to enhance the contrast. The self-focusing effect increases the laser intensity in the medium and enhances further more when the main pulse passing through it, while the ASE and noise peaks cannot have such effect. As a result, the intensity-enhanced main pulse increases the SD efficiency and improves the temporal contrast much more.

In this SD process, the generated SD1 signals are spatially separated from incident beams. There is no need of polarization discrimination device which will limit the temporal contrast improvement to five orders of magnitude at best. If there is any problem in the SD method, the surface and bulk scattering light from the nonlinear medium may limit the temporal contrast improvement. Fortunately, the scattering light has a much longer optical pass length in comparison with that of the main pulse. Then, these scattering lights from the main pulse will appear only in the postpulse. The surface scattering and bulk scattering are both at 10^{-4} level in K9 glass substrate. By using a crystalline bulk medium, the scattering is expected to be much reduced. The scattering light can also be reduced by propagating the SD1 beam for a longer distance or using a spatial filter. Thanks to the non-requirement of a polarizer, it is expected to improve the temporal contrast of laser pulse by more than 8 orders of magnitudes using SD process. In this way we are expecting to get the contrast of 10^{-14} relatively easily.

Figure 17(a) shows that the spectrum of the SD1 signal is clearly smoother with much less spike structures and broader than the input laser spectrum. The spectral phase is also smoothed for the SD1 signal. The spatial profile and beam quality of the SD1 signal were also improved in this SD process in comparison with the input laser beam owing to spatial filtering effect induced by self-focusing in the medium. The two-dimensional beam profiles of the SD1 signal are improved from an asymmetric incident beam to a nearly two-dimensional
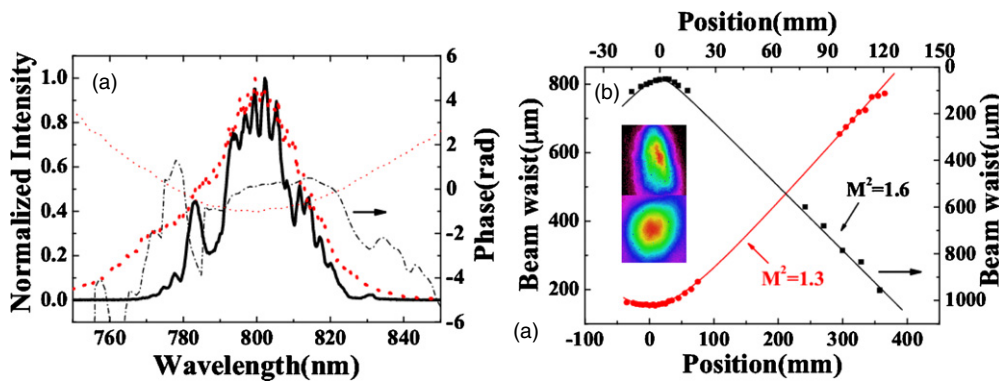

Figure 17. (a) Measured spectra of the incident pulse (black solid curve) and the SD1 signal (red dotted curve).The thin black dash-dotted curve and the thin magenta dotted curve show the retrieved spectra of the incident pulse and the SD1, respectively; (b) M^2 and two-dimensional beam profiles of the incident beam (black square curve, up pattern) and the SD1 signal (red circle curve, low pattern) [97].

isotropic and symmetric Gaussian beam, as illustrated in the inset of figure 17(b). The M^2 of the SD1 beam was also improved from 1.6 of the input laser beam to 1.3, as shown in figure 17(b).

These high-quality properties can be explained as follows. In a non-resonant electronic Kerr medium, the SD process is an instantaneous process only limited to femtosecond timescale determined by the pulse duration because of inertia-free interaction. The weak ASE with long lifetime and satellite pulses will experience SD processes separated from the main pulse in time. Moreover, by using the SD process, the SD signals are spatially separated from the two input beams. Therefore, there is no limit of improvement of temporal contrast due to the extinction ratio of the polarizer utilized in the XPW generation method. If the angular dispersion is not taken into consideration and the diffusive light from the Kerr medium is negligibly small in comparison with the noise in the SD pulse, the temporal contrast of the SD1 signal can be estimated as the cube of the temporal contrast of incident pulses $C_{SD1} \approx (C_{in})^3$ even in the picosecond range. Furthermore, the higher order SD signals have a much higher temporal contrast improvement from the time-domain expression: $I_{SD(m+1)}(t) \propto \int\int d\tau_2 I_1^{m+1}(t) I_1^{m+1}(t - \tau_1) I_2^{m+1}(t - \tau_2)$ which can be simplified to $I_{SD(m+1)} \propto (I_{SDm}(t))^2(t) I_{SD-1}(t - \tau)$ when the beam 1 and beam 2 have completely same temporal and spectral shapes from the same source and are perfectly overlapping in time. This relation also indicates that the pulse duration of the SD1 signal will be shortened in the SD process. In the frequency domain, the third-order dielectric polarization induced at a certain frequency ω_{SD1} is obtained by the sum over all possible permutations of fundamental frequencies weighted according to the third-order susceptibility. As a result, the intensity of the SD1 signal can be described as [57]

$$I_{SD1}(\omega_{SD1}) \propto \left| \int\int d\omega_1 d\omega_{-1} \tilde{E}_{-1}^*(z, \omega_{-1}) \tilde{E}_1(z, \omega_1) \tilde{E}_1(z, \omega_{SD1} \right.$$
$$\left. -\omega_{-1} + \omega_1) \sin c(\Delta k_z(\omega_{-1}, \omega_1, \omega_{SD1}, \omega_1, \omega_{-1}) L/2) \right|^2.$$

Here, ω_{SD1} and ω_1 and ω_{-1} are the angular frequencies of the SD1 signal, and the two incident beams, respectively. In the above equation, $\Delta k_z(\omega_{-1}, \omega_1, \omega_{SD1}, \omega_1, \omega_{-1})$ is the phase mismatch and L is the path length in the medium. As one can see from the equation, the spectrum of the SD1 signal is obtained by the double frequency integration of the spectral intensity of two incident laser pulses. It means that the intensity of the SD1 signal at each frequency component is an averaged contribution over the whole spectral region of the incident pulses. Therefore, the spectrum of the SD1 signal is smoothed automatically. Moreover, this averaged contribution makes the relative contribution of the central wavelength components be suppressed and that of the weak wings on both sides be enhanced. Simultaneously, from the phase-matching condition, new wavelength will be generated on both sides of the SD1 signal spectrum. As a result, the spectrum of the SD1 signal is broadened in accordance with the pulse narrowing explained in time domain as mentioned above. This SD process can take place in a wide spectral range
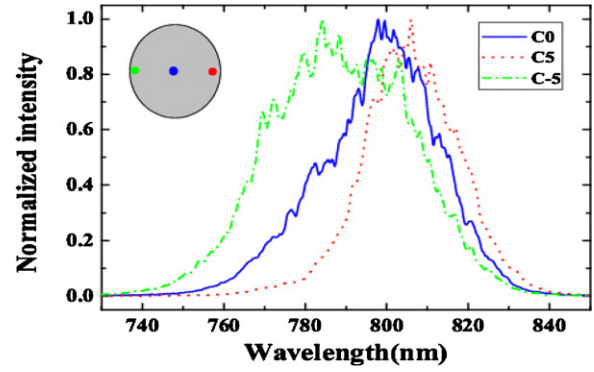

Figure 18. The SD spectra at the three different positions C0, C5 and C-5, respectively. The inset pattern shows the three different positions on the beam we measured. C0 is the centre of the beam. C5 and C-5 refer to the two positions located about 5 mm from the centre position C0. C-5 is the one closer to the incident beams [97].

with a broadband incident spectrum when the incident crossing angle is small and the medium is thin enough based on the description in the SD FROG measurement [57].

There is one concern regarding this method. It is the angular chirp of the generated SD signal inevitable in the finite angel configuration between the two incident beams as shown in figure 18. We can solve the problem by the following two steps. At first using a prism for each beam of first and minus-first order, the angular dispersion is converted to the parallel space-dispersed beam, as used in the pulse front tilting method [64]. Then combining the two beams by a beam-combiner (beam splitter), as a result the spatial dispersion in the opposite direction is cancelled. This pulse duration increase is reduced by the pulse front tilting [64] using a Brewster-angled prism in both arms with the minimum loss.

All of the above-mentioned outstanding performances make the SD an extremely useful method for the generation of a seed pulse in the designing of background-free petawatt laser systems in the future. Also, a high-quality intense pulse with high temporal contrast will be a powerful and useful source for a high intensity and stable attosecond pulse generation when it is focused onto the solid target surface.

Finally, the comparison of the mechanism of obtaining the clean pulse with CEP stabilization is shown. The former is explained by the fact that the output is proportional to the cubic of the incident pulse field, and it is essential to remove the contributions of weak satellite pulses and ASE. This is due to the *multiplication* process of *amplitude* in the nonlinear process. This is a high contrast to the CEP stabilization in which the *subtraction* process of the *phases* in the nonlinear process, which is given by the product of the complex amplitude of the relevant field, one of which is the complex conjugate, is essential in the removal of phase fluctuation.

5. Conclusion

Three basic methods developed in the femtosecond domain in the authors' group, which are useful and thought to be provoking for attosecond pulse generation, are described. The

14

J. Phys. B: At. Mol. Opt. Phys. **45** (2012) 074005

T Kobayashi *et al*

first method is the generation of CEP stable pulses. Sub-5 fs and sub-3 fs pulses with CEP stability by the passive mechanism are generated from a NOPA in the NIR and visible spectral range, respectively. The second method is the generation of multicolour pulses by CFWM in bulk media. This may be used for monocycle pulse generation by the Fourier sum method. The third one is a new technique based on the SD process in the Kerr medium, which is used to clean and optimize the femtosecond laser pulse. The cleaned pulse with high temporal contrast is expected to be useful as a seed for a background-free petawatt laser system and then used as the laser source for high-energy attosecond generation in a solid target.

The mechanism of obtaining the high-quality laser beams can be viewed as the application of *phase subtraction* and *amplitude addition and amplitude product* in the nonlinear processes for the improvement of the CEP stability and clean temporal, spectral and spatial properties.

Acknowledgments

References

[1] Ell R *et al* 2001 Generation of 5 fs pulses and octave-spanning spectra directly from a Ti:sapphire laser *Opt. Lett.* **26** 373–5

[2] Binhammer T, Rittweger E, Morgner U, Ell R and Kärtner F X 2006 Spectral phase control and temporal super-resolution toward the single-cycle pulse *Opt. Lett.* **31** 1552–4

[3] Matsubara E, Yamane K, Sekikawa T and Yamashita M 2007 Generation of 2.6 fs optical pulses using induced-phase modulation in a gas-filled hollow fiber *J. Opt. Soc. Am.* B **24** 985–9

[4] Shirakawa A, Sakane I, Takasaka M and Kobayashi T 1999 Sub-5 fs visible pulse generation by pulse-front-matched non-collinear optical parametric amplification *Appl. Phys. Lett.* **74** 2268–70

[5] Baltuška A, Fuji T and Kobayashi T 2002 Visible pulse compression to 4 fs by optical parametric amplification and programmable dispersion control *Opt. Lett.* **27** 306–8

[6] Strickland D and Mourou G 1985 Compression of amplified chirped optical pulses *Opt. Commun.* **56** 219–21
Maine P, Strickland D, Bado P, Pessot M and Mourou G 1988 Generation of ultrahigh peak power pulses by chirped pulse amplification *IEEE J. Quantum Electron.* **24** 398–403

[7] Ross I N, Matousek P, Towrie M, Langley A J and Collier J L 1997 The prospects for ultra-short pulse duration and ultra-high intensity using optical parametric amplifiers *Opt. Commun.* **144** 125–33

[8] Kiriyama H *et al* 2010 High temporal and spatial quality petawatt-class Ti:sapphire chirped-pulse amplification laser system *Opt. Lett.* **35** 1497–9

[9] Herrmann D, Veisz L, Tautz R, Tavella F, Schmid K, Pervak V and Krausz F 2009 Generation of sub-three-cycle, 16 TW light pulses by using noncollinear optical parametric chirped-pulse amplification *Opt. Lett.* **34** 2459–61

[10] Mikhailova J M, Buck A, Borot A, Schmid K, Sears Ch, Tsakiris G D, Krausz F and Veisz L 2011 Ultra-high-contrast few-cycle pulses for multipetawatt-class laser technology *Opt. Lett.* **36** 3145–7

[11] Witte S, Zinkstok R Th, Wolf A L, Hogervorst W, Ubachs W and Eikema K S E 2006 A source of 2 terawatt, 2.7 cycle laser pulses based on noncollinear optical parametric chirped pulse amplification *Opt. Express* **14** 8168–77

[12] Tzallas P, Skantzakis E, Nikolopoulos L A A and Tsakiris G D 2011 Extreme-ultraviolet pump–probe studies of one-femtosecond-scale electron dynamics *Nature* **7** 781–4

[13] Antoine Ph, L'Huillier A and Lewenstein M 1999 Attosecond pulse trains using high-order harmonics *Phys. Rev. Lett.* **77** 1234–7

[14] Paul P M, Toma E S, Breger P, Mullot G, Auge F, Balcou Ph, Muller H G and Agostini P 2001 Observation of train of attosecond pulses from high harmonic generation *Science* **292** 1689–92

[15] Tzallas P, Charalambidis D, Papadogiannis N A, Witte K and Tsakiris G D 2003 Direct observation of attosecond light bunching *Nature* **426** 267

[16] Nabekawa Y, Shimizu T, Okino T, Furusawa K, Hasegawa H, Yamanouchi K and Midorikawa K 2006 Conclusive evidence of an attosecond pulse train observed with the mode-resolved autocorrelation technique *Phys. Rev. Lett.* **96** 083901

[17] Brabec T and Krausz F 2000 Intense few-cycle laser fields: frontiers of nonlinear optics *Rev. Mod. Phys.* **72** 545–91

[18] Baltuška A *et al* 2003 Attosecond control of electronic processes by intense light fields *Nature* **421** 611

[19] Sansone G *et al* 2006 Isolated single-cycle attosecond pulses *Science* **314** 443–6

[20] Tzallas P, Skantzakis E, Kalpouzos C, Benis E P, Tsakiris G D and Charalambidis D 2007 Generation of intense continuum extreme-ultraviolet radiation by many-cycle laser fields *Nature Phys.* **3** 846–50

[21] Mashiko H, Gilbertson S, Li C Q, Khan S D, Shakya M M, Moon E and Chang Z H 2008 Double optical gating of high-order harmonic generation with carrier-envelope phase stabilized lasers *Phys. Rev. Lett.* **100** 103906

[22] Takahashi E J, Lan P, Mücke O D, Nabekawa Y and Midorikawa K 2010 Infrared two-color multicycle laser field synthesis for generating an intense attosecond pulse *Phys. Rev. Lett.* **104** 233901

[23] Ferrari F, Calegari F, Lucchini M, Vozzi C, Stagira S, Sansone G and Nisoli M 2010 High-energy isolated attosecond pulses generated by above-saturation few-cycle fields *Nature Photon.* **4** 875–9

[24] Tzallas P, Skantzakis E and Charalambidis D 2010 Measuring the absolute carrier-envelope phase of many-cycle laser fields *Phys. Rev.* A **82** 061401

[25] Kim K T, Kim C M, Baik M-G, Umesh G and Nam C H 2004 Single sub-50-attosecond pulse generation from chirp-compensated harmonic radiation using material dispersion *Phys. Rev.* B **69** 051805

[26] Ko D H, Kim K T, Park J, Lee J and Nam C H 2010 Attosecond chirp compensation over broadband high-order harmonics to generate near transform-limited 63 as pulses *New J. Phys.* **12** 063008

[27] Kalosha V P and Herrmann J 2000 Phase relations, quasicontinuous spectra and subfemtosecond pulses in high-order stimulated Raman scattering with short-pulse excitation *Phys. Rev. Lett.* **85** 1226

[28] Kalosha V, Spanner M, Herrmann J and Ivanov M 2002 Generation of single dispersion precompensated 1-fs pulses by shaped-pulse optimized high-order stimulated Raman scattering *Phys. Rev. Lett.* **88** 103901

[29] Sokolov A V, Shverdin M Y, Walker D R, Yavuz D D, Burzo A M, Yin G Y and Harris S E 2005 Generation and control of femtosecond pulses by molecular modulation *J. Mod. Opt.* **52** 285

[30] Shverdin M Y, Walker D R, Yavuz D D, Yin G Y and Harris S E 2005 Generation of a single-cycle optical pulse *Phys. Rev. Lett.* **94** 033904

[31] Dromey B *et al* 2006 High harmonic generation in the relativistic limit *Nature Phys.* **2** 456–9

[32] Hörlein R *et al* 2010 Temporal characterization of attosecond pulses emitted from solid-density plasmas *New J. Phys.* **12** 043020

[33] Tarasevitcha A and von der Linde D 2009 High order harmonic generation from solid targets: towards intense attosecond pulses *Eur. Phys. J. Spec. Top.* **175** 35–41

[34] Tsakiris G D, Eidmann K, Meyer-ter-Vehn J and Krausz F 2006 Route to intense single attosecond pulses *New J. Phys.* **8** 19

[35] Tarasevitch A P, Kohn R and von der Linde D 2009 Towards intense attosecond pulses: using two beams for high order harmonic generation from solid targets *J. Phys. B: At. Mol. Opt. Phys.* **42** 134006

[36] Mourou G, Tajima T and Bulanov S 2006 Optics in the relativistic regime *Rev. Mod. Phys.* **78** 309

[37] Apolonski A, Poppe A, Tempea G, Spielmann C, Udem T, Holzwarth R, Hänsch T W and Krausz F 2000 Controlling the phase evolution of few-cycle light pulses *Phys. Rev. Lett.* **85** 740

[38] Drescher M, Hentshel M, Kienberger R, Tempea G, Spielmann C, Reider G, Corkum P and Krausz F 2001 X-ray pulses approaching the attosecond frontier *Science* **291** 1923

[39] Jones D J, Diddams S A, Ranka J K, Stentz A, Windeler R S, Hall J L and Cundiff S T 2000 Carrier-envelope phase control of femtosecond mode-locked lasers and direct optical frequency synthesis *Science* **288** 635

[40] Kobayashi Y and Torizuka K 2001 Carrier-phase control among subharmonic pulses in a femtosecond optical parametric oscillator *Opt. Lett.* **26** 1295–7

[41] Helbing F W, Steinmeyer G, Keller U, Windeler R S, Stenger J and Tulle H R 2002 Carrier-envelope offset dynamics of mode-locked lasers *Opt. Lett.* **27** 194–6

[42] Paulus G G, Grasbon F, Walther H, Villoresi P, Nisoli M, Stagira S, Priori E and De Silvestri S 2001 Absolute-phase phenomena in photoionization with few-cycle laser pulses *Nature* **414** 182

[43] Baltuška A, Fuji T and Kobayashi T 2002 Controlling the carrier-envelope phase of ultrashort light pulses with optical parametric amplifiers *Phys. Rev. Lett.* **88** 133901

[44] Fang X and Kobayashi T 2004 Self-stabilization of carrier-envelope phase of an optical parametric amplifier verified by with a photonic crystal fiber *Opt. Lett.* **29** 1282–4

[45] Zimmermann M, Gohle C, Holzwarth R, Udem Th and Hänsch T W 2004 Optical clockwork with an offset-free difference-frequency comb: accuracy of sum- and difference-frequency generation *Opt. Lett.* **29** 310

[46] Adachi S, Kumbhakar P and Kobayashi T 2004 Quasi-monocyclic near-infrared pulses with a stabilized carrier-envelope phase characterized by noncollinear cross-correlation frequency-resolved optical gating *Opt. Lett.* **29** 1150–2

[47] Shirakawa A and Kobayashi T 1998 Noncollinearly phase-matched femtosecond optical parametric amplification with a 2000 cm^{-1} bandwidth *Appl. Phys. Lett.* **72** 147–9

[48] Cerullo G, Nisoli M, Stagira S and Silvestri S De 1998 Sub-8-fs pulses from an ultrabroadband optical parametric amplifier in the visible *Opt. Lett.* **23** 1283–5

[49] Riedle E, Beutter M, Lochbrunner S, Piel J, Schenkl S, Spoerlein S and Zinth W 2000 Generation of 10 to 50 fs pulses tunable through all of the visible and the NIR *Appl. Phys.* B **71** 457

[50] Kobayashi T and Shirakawa A 2000 Tunable visible and near-infrared pulse generator in a 5 fs regime *Appl. Phys.* B **70** S239

[51] Zavelani-Rossi M, Cerullo G, De Silvestri S, Gallmann L, Matuschek N, Steinmeyer G, Keller U, Angelow G, Scheuer V and Tschudi T 2001 Pulse compression over a 170-THz bandwidth in the visible by use of only chirped mirrors *Opt. Lett.* **26** 1155–7

[52] Baltuška A and Kobayashi T 2002 Adaptive shaping of two-cycle visible pulses using a flexible mirror *Appl. Phys.* B **75** 427

[53] Linden S, Giessen H and Kuhl J 1998 XFROG-a new method for amplitude and phase characterization of weak ultrashort pulses *Phys. Status Solidi* b **206** 119

[54] Linden S, Kuhl J and Giessen H 1999 Amplitude and phase characterization of weak blue ultrashort pulses by downconversion *Opt. Lett.* **24** 569–71

[55] Saikan S, Ouw D and Schäfer P 1979 Automatic phase-matched frequency-doubling system for the 240–350 nm region *Appl. Opt.* **18** 193

[56] Szabó G and Bor Z 1994 Frequency conversion of ultrashort pulses *Appl. Phys.* B **58** 237

[57] Trebino R and Kane D J 1993 Using phase retrieval to measure the intensity and phase of ultrashort pulses frequency-resolved optical gating *J. Opt. Soc. Am.* A **10** 1101

[58] Baltuška A, Pshenichnikov M S, Wiersma D A and Szipocs R ed R Kaarli, A Freiberg and P Saari 1998 *Ultrafast Processes in Spectroscopy* (Tartu, Estonia: Institute of Physics, University of Tartu) p 7

[59] Okamura K and Kobayashi T 2011 Octave-spanning carrier-envelope phase stabilized visible pulse with sub-3-fs pulse duration *Opt. Lett.* **36** 226–8

[60] Adachi S and Kobayashi T 2005 Carrier-envelope phase-controlled quantum interference in optical poling *Phys. Rev. Lett.* **94** 153903

[61] Okamura K and Kobayashi T 2008 Carrier-envelope phase measurement by all-optical poling with a polar side-chain polymer *Opt. Commun.* **281** 5870

[62] Szabó G and Bor Z 1990 Broadband frequency doubler for femtosecond pulses *Appl. Phys. B* **50** 51

[63] Kanai T, Zhou X, Sekikawa T, Watanabe S and Togashi T 2003 Generation of subterawatt sub-10 fs blue pulses at 1–5 kHz by broadband frequency doubling *Opt. Lett.* **28** 1484

[64] Shirakawa A, Sakane I and Kobayashi T 1998 Pulse-front-matched optical parametric amplification for sub-10 fs pulse generation tunable in the visible and near infrared *Opt. Lett.* **23** 1292–4

[65] Zhi M and Sokolov A V 2007 Broadband coherent light generation in a Raman-active crystal driven by two-color femtosecond laser pulses *Opt. Lett.* **32** 2251–3

[66] Zhi M and Sokolov A V 2008 Broadband generation in a Raman crystal driven by a pair of time-delayed linearly chirped pulses *New J. Phys.* **10** 025032

[67] Inoue K, Kato J, Hanamura E, Matsuki H and Matsubara E 2007 Broadband coherent radiation based on peculiar multiple Raman scattering by laser-induced phonon grating in TiO$_2$ *Phys. Rev.* B **76** 041101

[68] Matsubara E, Sekikawa T and Yamashita M 2008 Generation of ultrashort optical pulses using multiple coherent anti-Stokes Raman scattering in a crystal at room temperature *Appl. Phys. Lett.* **92** 071104

[69] Matsuki H, Inoue K and Hanamura E 2007 Multiple coherent anti-Stokes Raman scattering due phonon grating in

KNbO$_3$ induced by crossed beams of two-color femtosecond pulses *Phys. Rev.* B **75** 024102

[70] Takahashi J, Mano K and Yano T 2006 Raman lasing and cascaded coherent anti-Stokes Raman scattering of a two-phonon Raman band *Opt. Lett.* **31** 1501–3

[71] Matsubara E, Inoue K and Hanamura E 2005 Violation of Raman selection rules induced by two femtosecond laser pulses in KTaO$_3$ *Phys. Rev.* B **72** 134101

[72] Matsubara E, Kawamoto Y, Sekikawa T and Yamashita M 2009 Generation of ultrashort optical pulses in the 10 fs regime using multicolor Raman sidebands in KTaO$_3$ *Opt. Lett.* **34** 1837–9

[73] Takahashi J, Matsubara E, Arima T and Hanamura E 2003 Coherent multistep anti-Stokes and stimulated Raman scattering associated with third harmonics in YFeO$_3$ crystals *Phys. Rev.* B **68** 155102

[74] Zhi M, Wang X and Sokolov A V 2008 Broadband coherent light generation in diamond driven by femtosecond pulses *Opt. Express* **16** 12139–47

[75] Liu J, Zhang J and Kobayashi T 2008 Broadband coherent anti-Stokes Raman scattering light generation in BBO crystal by using two crossing femtosecond laser pulses *Opt. Lett.* **33** 1494–6

[76] Crespo H, Mendonça J T and Dos Santos A 2000 Cascaded highly nondegenerate four-wave-mixing phenomenon in transparent isotropic condensed media *Opt. Lett.* **25** 829–31

[77] Weigand R, Mendonca J T and Crespo H 2009 Cascaded nondegenerate four-wave mixing technique for high-power single-cycle pulse synthesis in the visible and ultraviolet ranges *Phys. Rev.* A **79** 063838

[78] Silva J L, Weigand R and Crespo H 2009 Octave-spanning spectra and pulse synthesis by non-degenerate cascaded four-wave mixing *Opt. Lett.* **34** 2489–91

[79] Liu J and Kobayashi T 2009 Wavelength-tunable multicolored femtosecond laser pulse generation in fused silica glass *Opt. Lett.* **34** 1066–8

[80] Liu J and Kobayashi T 2009 Generation of uJ-level multicolored femtosecond laser pulses using cascaded four-wave mixing *Opt. Express* **17** 4984–90

[81] Liu J and Kobayashi T 2008 Cascaded four-wave mixing and multicolored arrays generation in a sapphire plate by using two crossing beams of femtosecond laser *Opt. Express* **16** 22119–25

[82] Liu J and Kobayashi T 2009 Generation of sub-20-fs multicolor laser pulses using cascaded four-wave mixing with chirped incident pulses *Opt. Lett.* **34** 2402–4

[83] Liu J and Kobayashi T 2010 Cascaded four-wave mixing in transparent bulk media *Opt. Commun.* **283** 1114–23

[84] Liu J, Kida Y, Teramoto T and Kobayashi T 2010 Simultaneous compression and amplification of a laser pulse in a glass plate *Opt. Express* **18** 2495–502

[85] Liu J, Kobayashi T and Wang Z G 2009 Generation of broadband two-dimensional multicolored arrays in a sapphire plate *Opt. Express* **17** 9226–34

[86] Strelkov V V, Mével E and Constant E 2008 Generation of isolated attosecond pulses by spatial shaping of a femtosecond laser beam *New J. Phys.* **10** 083040

[87] Ferrari F, Calegari F, Lucchini M, Vozzi C, Stagira S, Sansone G and Nisoli M 2010 High-energy isolated attosecond pulses generated by above-saturation few-cycle fields *Nature Photon.* **4** 875–9

[88] Quéré F, Thaury C, Monot P, Dobosz S, Martin P, Geindre J-P and Audebert P 2006 Coherent wake emission of high-order harmonics from overdense plasmas *Phys. Rev. Lett.* **96** 125004

[89] Dromey B *et al* 2009 Diffraction-limited performance and focusing of high harmonics from relativistic plasmas *Nature Phys.* **5** 146–52

[90] Antici P *et al* 2007 Energetic protons generated by ultrahigh contrast laser pulses interacting with ultrathin targets *Phys. Plasmas* **14** 030701

[91] Yanovsky V *et al* 2008 Ultra-high intensity- 300-TW laser at 0.1 Hz repetition rate *Opt. Express* **16** 2109–14

[92] Chvykov V, Rousseau P, Reed S, Kalinchenko G and Yanovsky V 2006 Generation of 10^{11} contrast 50 TW laser pulses *Opt. Lett.* **31** 1456–8

[93] Jullien A *et al* 2005 10^{-10} temporal contrast for femtosecond ultraintense lasers by cross-polarized wave generation *Opt. Lett.* **30** 920–2

[94] Cotel A, Jullien A, Forget N, Albert O, Cheriaux G and Le Blanc C 2006 Nonlinear temporal pulse cleaning of a 1 mu m optical parametric chirped-pulse amplification system *Appl. Phys.* B **83** 7–10

[95] Schneider T, Wolfframm D, Mitzner R and Reif J 1999 Ultrafast optical switching by instantaneous laser-induced grating formation and self-diffraction in barium fluoride *Appl. Phys.* B **68** 749–51

[96] DeLong K W, Trebino R, Hunter J and White W E 1994 Frequency-resolved optical gating with the use of second-harmonic generation *J. Opt. Soc. Am.* B **11** 2206–15

[97] Liu J, Okamura K, Kida Y and Kobayashi T 2010 Temporal contrast enhancement of femtosecond pulses by a self-diffraction process in a bulk Kerr medium *Opt. Express* **18** 22245–54